Research Square

Preprints are preliminary reports that have not undergone peer review.
They should not be considered conclusive, used to inform clinical practice,
or referenced by the media as validated information.

Study on the Removal Performance and Mechanism of U(VI) from Rare Earth Wastewater Using Phytic Acid-Crosslinked Chitosan@Attapulgite Composites

Xin Wang
University of South China
Huayong Huang
University of South China
Shuiyun Wang
Nonferrous Metallurgy Design and Research Institute
Wenxuan Tang
University of South China
Qinquan Liu
University of South China
Shuibo Xie
xiesbmr@263.net
University of South China

Research Article

Keywords:

Posted Date: November 20th, 2026

DOI: https://doi.org/10.21203/rs.3.rs-11546015/v1

License: This work is licensed under a Creative Commons Attribution 4.0 International License.
Read Full License

Additional Declarations: No competing interests reported.

Study on the Removal Performance and Mechanism of U(VI) from Rare Earth Wastewater Using Phytic Acid-Crosslinked Chitosan@Attapulgite Composites

Xin Wang[1], Huayong Huang[1,2], Shuiyun Wang[3], Wenxuan Tang[1], Qinquan Liu[1], Shuibo Xie[1,2]*

[1] School of Civil Engineering, University of South China, Hengyang 421001, Hunan, China

[2] Key Discipline Laboratory for National Defence of Biotechnology in Uranium Mining and Hydrometallurgy, University of South China, Hengyang 421001, People's Republic of China

[3] Nonferrous Metallurgy Design and Research Institute, Changsha 410000, China

Abstract

Deep removal of U(VI) from uranium-bearing rare-earth wastewater is difficult for conventional adsorbents: uranium occurs only at trace concentrations, while coexisting ions such as Ca^{2+} and K^{+} interfere strongly with adsorption. A phytic acid-crosslinked chitosan/attapulgite composite (ATP-CS-PA) was prepared by blending, using phytic acid (PA) as the crosslinking agent. The best performance was obtained at an ATP:CS:PA mass ratio of 3:10:10. At an initial U(VI) concentration of 10.00 mg/L, an adsorbent dosage of 0.10 g/L, pH 5.0 and 298 K, adsorption reached equilibrium within 120 min with a capacity of 98.34 mg/g. The maximum capacity obtained from the Langmuir model was 526.16 mg/g. Adsorption was attributed mainly to inner-sphere coordination with phosphate groups. As a hard Lewis acid, UO_2^{2+} preferentially coordinates with phosphate groups to form P–O–U bonds, with amino and surface hydroxyl groups also contributing. The composite retained high selectivity in the presence of coexisting ions, including Ca^{2+} and Fe^{3+} at 10–100 mg/L, and achieved a uranium removal rate of 83.48% after five adsorption–desorption cycles. Treatment of rare-earth wastewater containing 0.30 mg/L U(VI) reduced its concentration to 0.02 mg/L, meeting the limit specified in GB 26451–2011.

1 Introduction

Leaching of ion-adsorption rare-earth ores mobilizes associated uranium and produces substantial quantities of rare-earth wastewater containing uranium at low concentrations [1]. Uranium occurs mainly as UO_2^{2+} and its hydrolysis products. The Chinese Discharge Standards of Pollutants for the Rare Earths Industry (GB 26451–2011) limit the combined concentration of thorium and uranium to 0.10 mg/L. Conventional adsorbents struggle to achieve deep U(VI) removal in complex ionic matrices.

Chitosan (CS) contains abundant amino and hydroxyl groups that provide coordination sites for uranyl ions [2]. However, its selectivity and adsorption capacity are limited in rare-earth wastewater with low uranium concentrations, high salinity and multiple coexisting ions [3]. Unmodified CS also has a low specific surface area and poor mechanical strength and is prone to dissolution under acidic conditions [4]. Attapulgite (ATP) has a high specific surface area, mechanical strength and chemical stability [5]. Combining ATP with CS has been reported to improve U(VI) removal [6]. Phytic acid (PA) contains six phosphate groups and has been used in phytic acid–chitosan–graphene oxide [7] and phytic acid–chitosan/sodium alginate systems [8]. However, a ternary composite constructed by crosslinking with PA and using inexpensive ATP as a framework has not, to our knowledge, been reported.

In this study, PA was used as both a crosslinker and a functional component to prepare ATP-CS-PA by blending. The multiple phosphate groups of PA crosslink with CS amino groups to form a three-dimensional network, which suppresses CS dissolution under acidic conditions and provides abundant phosphate coordination sites. ATP acts as a rigid framework that can improve dispersion and pore structure. The effects of solution pH, adsorbent dosage, initial concentration and coexisting ions on U(VI) adsorption were systematically investigated, and the adsorption mechanism was examined.

2 Materials, preparation and characterization

2.1 Materials and reagents

Chitosan (CS, 95% degree of deacetylation), attapulgite (ATP), phytic acid (PA, 50 wt%) and glacial acetic acid (CH_3COOH) were purchased from Shanghai Macklin Biochemical Co., Ltd. Triuranium octoxide (U_3O_8) was supplied by China National Nuclear Corporation 404. All chemicals were of analytical grade.

2.2 Preparation of ATP-CS-PA

ATP (5.0 g) was dispersed in 100 mL of 5% hydrochloric acid and stirred at 60 °C for 5 h. The solid was centrifuged, washed to neutrality and dried at 60 °C to constant mass to obtain acid-pretreated ATP. CS (1.0 g) was dissolved in 50 mL of 2% acetic acid and stirred at 60 °C for 1 h. Separately, 0.3 g of pretreated ATP was dispersed in 10 mL of deionized water and ultrasonicated for 25 min.

The ATP suspension was added dropwise to the CS solution, followed by stirring for 1 h. A mixture of 2.0 mL of 50% PA and 2.0 mL of deionized water was then added, and the mixture was stirred at 60 °C for 4 h. The pH was adjusted to 5.0 with 1 mol/L NaOH, and the mixture was left to gel for 12 h. It was washed with deionized water to neutrality and freeze-dried for 24 h to obtain ATP-CS-PA. An orthogonal experiment established an optimum ATP:CS:PA feed mass ratio of 3:10:10.

2.3 Characterization

The surface morphologies of CS, ATP-CS and ATP-CS-PA were examined by scanning electron microscopy (SEM; Apreo 2, USA). Energy-dispersive X-ray spectroscopy (EDS; X-Max, UK) was used to determine the elemental compositions of CS, ATP-CS and ATP-CS-PA before and after adsorption. Fourier transform infrared spectroscopy (FTIR; Nicolet iS10, USA) was used to examine functional groups in CS, ATP-CS, ATP-CS-PA and uranium-loaded ATP-CS-PA (ATP-CS-PA-U). X-ray diffraction (XRD; SmartLab 9, Japan) was used to characterize the crystalline structures of CS, ATP, ATP-CS and ATP-CS-PA. A surface-area analyzer (Micromeritics, USA) was used to determine the specific surface area and pore-size distribution. X-ray photoelectron spectroscopy (XPS; Escalab 250Xi, USA) was used to compare the surface functional groups of ATP-CS-PA before and after adsorption.

2.4 Adsorption experiments

Batch equilibrium experiments were conducted to evaluate adsorption. The solution pH was adjusted to within ±0.05 of the target value using 0.1 mol/L NaOH or HCl. A specified volume of U(VI) solution at a known initial concentration and a known mass of adsorbent were placed in a 50 mL conical flask and shaken at 150 r/min in a temperature-controlled shaker. After adsorption, the suspension was filtered through a 0.45 μm membrane, and the residual uranium concentration in the supernatant was measured by UV–visible spectrophotometry

(UV2700, Japan) at 578 nm. The concentrations of U(VI) and coexisting ions in actual wastewater before and after adsorption were measured by inductively coupled plasma optical emission spectrometry (ICP-OES). All experiments were performed in triplicate, and the mean values are reported.

The effects of the following variables were examined: initial pH of 2.0–7.0; adsorbent mass of 1–10 mg (equivalent to 0.02–0.20 g/L); initial U(VI) concentrations of 5, 10 and 15 mg/L for kinetic experiments and 5–80 mg/L for isotherm experiments; temperatures of 298, 308 and 318 K; and coexisting K^+, NH_4^+, Mg^{2+}, Ca^{2+}, Fe^{3+}, NO_3^-, SO_4^{2-} and CO_3^{2-} at 10–100 mg/L. Regeneration was evaluated over five consecutive adsorption–desorption cycles using 1 mol/L HCl as the desorbent.

2.5 Morphology and elemental composition of ATP-CS-PA

The synthesis route for ATP-CS-PA is shown in Fig. 1. CS dissolved in glacial acetic acid was first blended with acid-pretreated ATP. PA was then added to crosslink the mixture and induce gelation, followed by freeze-drying to obtain the porous composite.

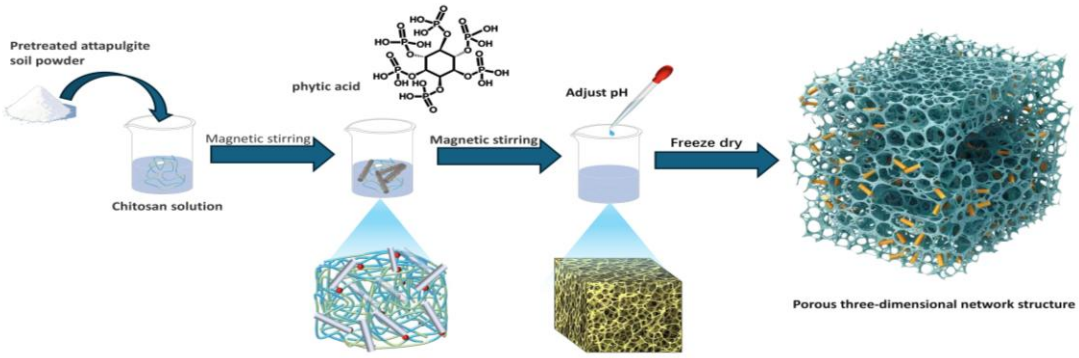

Fig. 1 Schematic illustration of the synthesis of ATP-CS-PA

SEM images of ATP, CS, ATP-CS and ATP-CS-PA are shown in Fig. 2.

Pristine ATP consisted of short rod-like crystal bundles stacked in a disordered arrangement (Fig. 2a) [5], whereas CS had a flat, smooth surface (Fig. 2b). The surface of ATP-CS (Fig. 2c) was distinctly rougher than that of CS and bore numerous needle-like features, attributed to rod-like ATP aggregates on the CS surface. The surface of ATP-CS-PA (Fig. 2d) was rougher than that of ATP-CS, with smaller particles evenly distributed across the CS surface. Its pore structure also changed, with more numerous, smaller and more closely spaced pores.

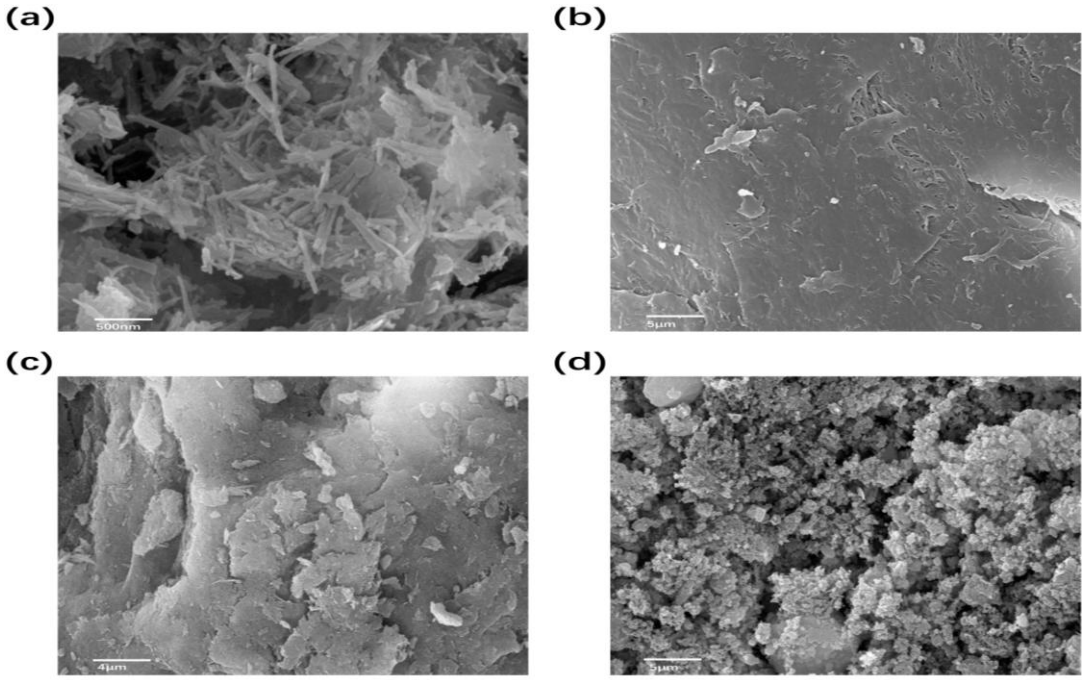

Fig. 2 SEM images of (a) ATP, (b) CS, (c) ATP-CS and (d) ATP-CS-PA

EDS provided elemental evidence for composite formation. Compared with CS (Fig. 3a), ATP-CS (Fig. 3b) showed a higher oxygen content, a lower nitrogen content and new Mg, Al and Si signals, originating from the aluminosilicate framework of ATP. The stronger P signal in ATP-CS-PA (Fig. 3c) further supported the incorporation of PA into the composite.

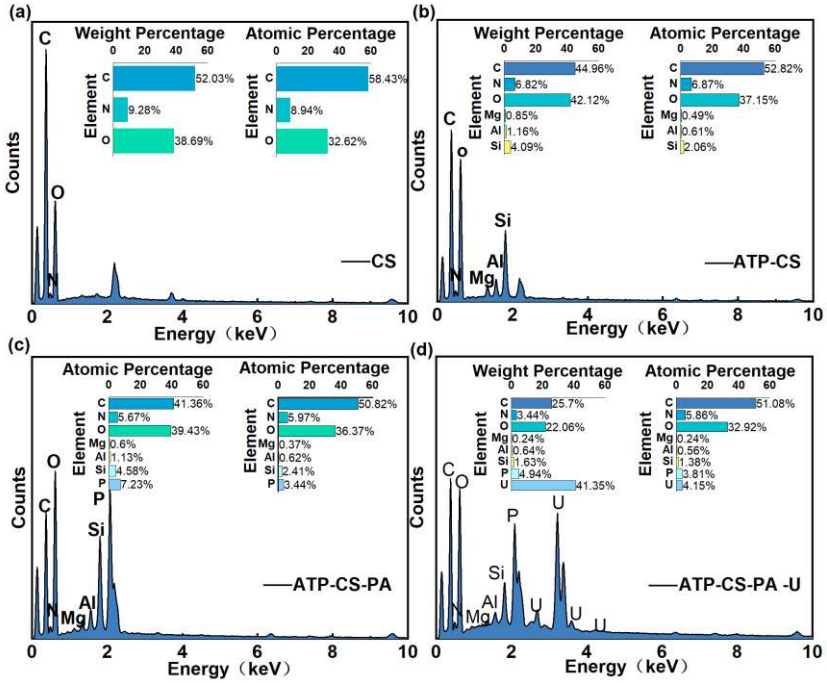

Fig. 3 EDS spectra of CS, ATP-CS and ATP-CS-PA before and after U(VI) adsorption
(a) CS; (b) ATP-CS; (c) ATP-CS-PA; (d) ATP-CS-PA after U(VI) adsorption

After adsorption, the surface was covered by fine particles and became rougher (Fig. 4a). A distinct U characteristic peak near 3.17 keV appeared in the EDS spectrum (Fig. 3d), confirming uranium loading. Elemental mapping (Fig. 4b) showed a uniform distribution of U without local enrichment or aggregation, with substantial overlap between the U, P and N

distribution regions.

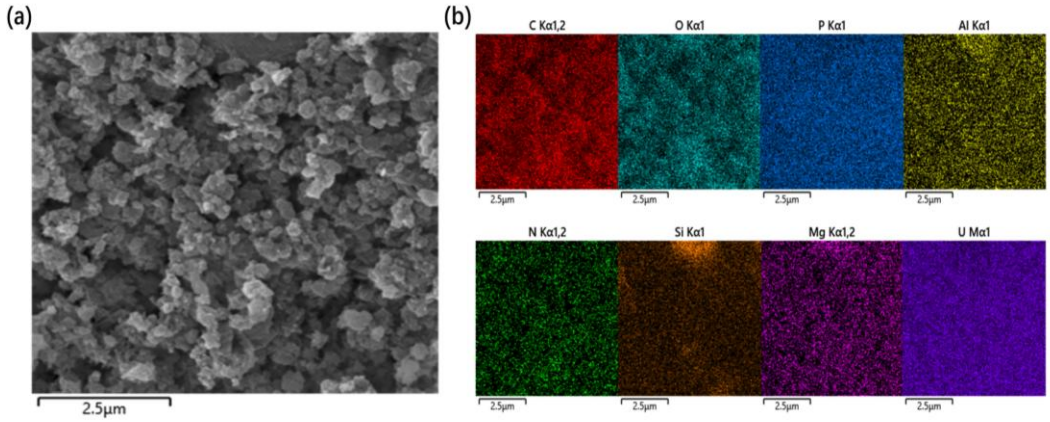

Fig. 4 ATP-CS-PA after U(VI) adsorption: (a) SEM image and (b) elemental maps

2.6 Crystalline structure of ATP-CS-PA

XRD was used to assess the state of the components in the composite (Fig. 5a). ATP showed sharp characteristic peaks at 2θ = 8.42°, 13.8° and 19.8°, assigned to the (110), (200) and (040) planes of attapulgite, respectively (PDF no. 21-0958). The peak at 2θ = 26.64° corresponded to the (101) plane of quartz (SiO_2), indicating a small amount of quartz impurity. Pure CS showed only a broad diffuse peak at approximately 2θ = 20°, characteristic of a semicrystalline polymer. The positions and intensities of the ATP peaks remained essentially unchanged after composite formation, suggesting that CS and PA did not disrupt the ATP crystalline framework. The components were interpreted as being combined through surface loading, with PA dispersed in an amorphous state and no new crystalline phase formed.

2.7 Surface functional groups of ATP-CS-PA

FTIR provided further evidence concerning the functional groups (Fig. 5b). Compared with pure ATP, the ATP-CS spectrum retained both the Si–O–Si framework vibration of ATP (approximately 1030 cm^{-1}) [9] and the amide I band (approximately 1640 cm^{-1}) and C–H vibration (approximately 2825 cm^{-1}) of CS, supporting successful composite formation. In ATP-CS-PA, the characteristic P–O–C/P=O absorption overlapped with the Si–O band at approximately 1000–1100 cm^{-1}, substantially broadening the band. A P–O shoulder also appeared near 500 cm^{-1}, indicating incorporation of PA. After adsorption, the intensities of the P–O bands at approximately 1085 and 950 cm^{-1} changed [10], as did the N–H and amide C=O bands at approximately 1640 and 1540 cm^{-1} [11]. These changes indicate altered chemical environments around phosphate and amino groups and are consistent with their participation in UO_2^{2+} coordination. The shifts in P 2p and N 1s binding energies observed by XPS provide complementary evidence for a chemical contribution to uranium uptake.

2.8 Pore structure and specific surface area of ATP-CS-PA

The specific surface area and pore-size distribution affect UO_2^{2+} mass transfer and the accessibility of active sites. As shown in Fig. 5c, the N_2 adsorption–desorption isotherms of both ATP-CS and ATP-CS-PA were type IV with H3 hysteresis loops, indicating predominantly mesoporous structures [12]. ATP-CS-PA exhibited greater adsorption than ATP-CS at high relative pressures, suggesting that PA modification increased porosity. The pore-size distributions of both materials ranged from 2 to 50 nm (Fig. 5d). The main peak at 3–4 nm and the broad peak at 10–40 nm were attributed to packing pores between attapulgite rod crystals

and between particles, respectively [13]. Both materials had a most probable pore diameter of 3.8 nm, suggesting that PA did not alter the inherent pore size. As shown in Table 1, the introduction of PA substantially increased the specific surface area and the proportion of mesopores [14], while microporosity changed little. This suggests that PA inhibited the close packing of attapulgite rod crystals [15], forming a loosely packed coating and shifting the material from a predominantly microporous to a predominantly mesoporous structure.

Table 1 Pore structure parameters of CS, ATP-CS and ATP-CS-PA

Material	Surface area (m^2/g)	Micropore volume (cm^3/g)	Micropore area (m^2/g)	Mean pore diameter (nm)
CS	2.5	0.00086	1.73	7.3
ATP-CS	15.9	0.00261	6.29	7.96
ATP-CS-PA	92.8	0.00274	8.52	13.68

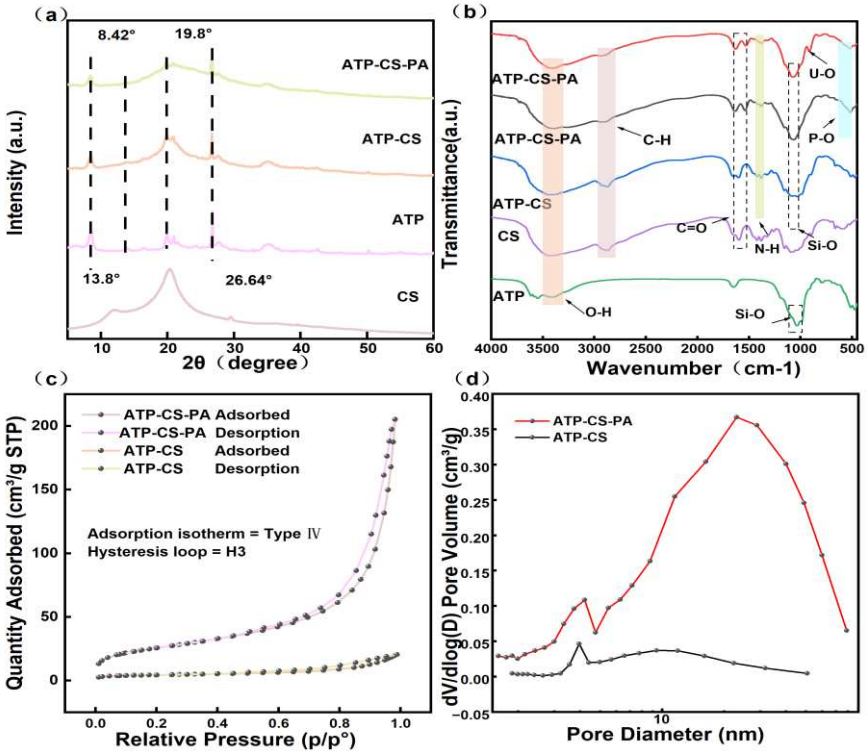

Fig. 5 (a) XRD patterns and (b) FTIR spectra of ATP, CS, ATP-CS and ATP-CS-PA; (c) N_2 adsorption–desorption isotherms and (d) pore-size distributions of ATP-CS and ATP-CS-PA

2.9 Surface chemical states of ATP-CS-PA

High-resolution XPS core-level spectra were used to characterize the surface chemical states and functional groups of ATP-CS-PA. The C 1s spectrum was resolved into C–O (285.9 eV), C=O (287.3 eV) and C–C (284.4 eV) components (Fig. 6a) [7], attributed mainly to carbon in CS and PA and surface-adsorbed hydrocarbons. The O 1s spectrum was fitted with three peaks (Fig. 6b), assigned to P–O in PA (532.86 eV) [16], P=O in PA phosphate groups (531.80 eV), and O–H in CS (533.6 eV) [17]. The N 1s spectrum contained signals assigned to CS amino groups, $–NH_2$ (399.12 eV) and NH_3 (401.37 eV), supporting the presence of CS in the composite (Fig. 6c) [18]. The P 2p spectrum showed a characteristic spin–orbit doublet (Fig. 6d), with P $2p_{3/2}$ at 133.25 eV and P $2p_{1/2}$ at 134.22 eV, assigned to phosphate groups in PA (PO_4^{3-}/HPO_4^{2-}) [8]. These binding energies are consistent with reported organic phosphates and

support PA incorporation.

XPS after adsorption provided evidence for the participation of functional groups in coordination. A new U=O peak at 530.44 eV appeared in the O 1s spectrum (Fig. 6b), indicating uranium loading [19]. The P–O and P=O components shifted from 532.09 and 531.80 eV to 532.80 and 531.50 eV, respectively, while the O–H component shifted from 533.60 to 533.48 eV, a change of 0.12 eV, consistent with the participation of surface hydroxyl groups (Si–OH, Al–OH and Mg–OH) in uranium coordination [20]. In the N 1s spectrum (Fig. 6c), the NH_3 and NH_2 components shifted from 401.47 and 399.12 eV to 401.63 and 399.38 eV, respectively, corresponding to shifts of 0.16 and 0.26 eV. In the P 2p spectrum (Fig. 6d), peaks initially at 133.16 and 134.07 eV shifted by 0.09 and 0.15 eV, respectively, and broadened slightly, suggesting interactions between PA phosphate groups and UO_2^{2+} [21]. The U $4f_{7/2}$ and U $4f_{5/2}$ peaks appeared at 381.83 and 392.76 eV, respectively (Fig. 6e), with a spin–orbit separation of 10.93 eV, consistent with reported U(VI) binding energies [22]. The survey spectrum (Fig. 6f) showed a distinct U signal after adsorption, whereas the C, N, O, P and Si signals remained present, consistent with retention of the composite's basic composition. XPS shift magnitude reflects the sensitivity of each group to changes in its electronic environment and cannot by itself quantify the group's contribution to adsorption capacity.

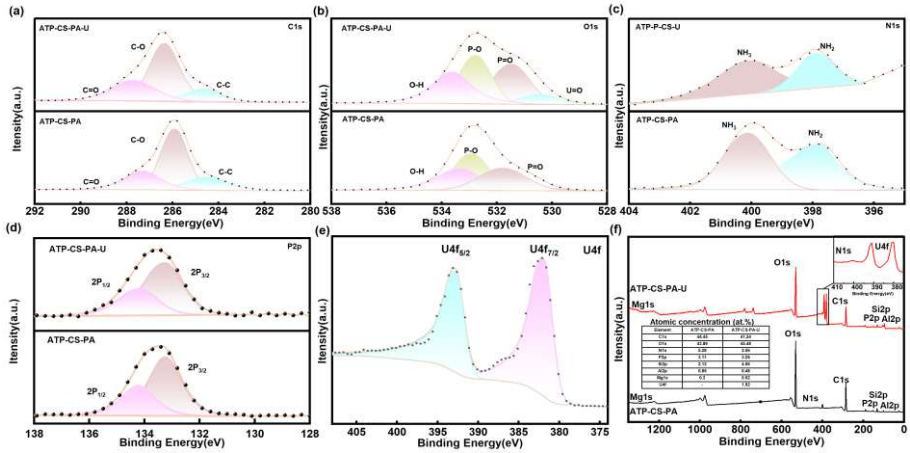

Fig. 6 XPS spectra of ATP-CS-PA before and after U(VI) adsorption: (a) C 1s, (b) O 1s, (c) N 1s, (d) P 2p, (e) U 4f and (f) survey spectra

3 Adsorption performance

3.1 Effect of pH on U(VI) adsorption

Solution pH affects uranium speciation and adsorption. Fig. 7a shows the effect of pH on uranium adsorption by the three materials. Over pH 2.0–7.0, the adsorption capacities of CS, ATP-CS and ATP-CS-PA increased with pH. At pH 2.0, the surfaces were highly protonated, leading to electrostatic repulsion with U(VI) and low adsorption. ATP-CS-PA reached its highest capacity of 98.34 mg/g at pH 5.0 and maintained capacities above 93.00 mg/g over pH 5.0–7.0, exceeding those of CS and ATP-CS. The largest differences occurred at pH 2.0–4.0; at pH 2.0, the capacities of CS, ATP-CS and ATP-CS-PA were 1.7, 3.4 and 46.9 mg/g, respectively. These results were attributed to the dual role of PA: its phosphate groups crosslink with CS amino groups to form a network that retains structural integrity over a broad pH range, while functional phosphate groups can coordinate UO_2^{2+} through P–O–U bonds at pH 5.0–7.0. CS amino groups may contribute through N–U coordination [23]. Together, these effects improve the adsorption performance and selectivity of CS under acidic conditions.

3.2 Effect of adsorbent dosage on U(VI) adsorption

The effect of ATP-CS-PA dosage on U(VI) removal is shown in Fig. 7b. As the dosage increased from 0.02 to 0.08 g/L, removal rose rapidly from 71.62% to 98.34%. A further increase to 0.20 g/L improved removal by less than 1.4 percentage points, to 99.69%. The equilibrium adsorption capacity decreased from 358.1 to 49.8 mg/g, a reduction of 86.1%, because the amount of U(VI) available in solution was limited. Particle aggregation and overlapping sites may also have reduced site accessibility [24]. A dosage of 0.10 g/L was selected for subsequent experiments.

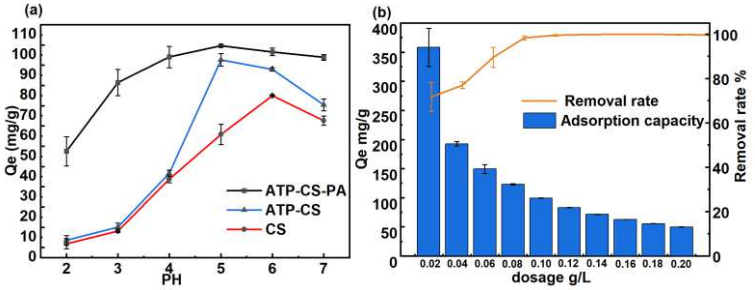

Fig. 7 Effects of (a) pH and (b) adsorbent dosage on uranium adsorption by ATP-CS-PA

3.3 Adsorption kinetics

Fig. 8a shows the adsorption capacity of ATP-CS-PA as a function of time at initial U(VI) concentrations of 5, 10 and 15 mg/L. The three curves rose rapidly during the first 20 min, reaching 49.38, 94.81 and 125.45 mg/g, respectively, and approached equilibrium after 60 min. The initial rapid uptake was attributed to abundant available sites and a strong mass-transfer driving force; the rate subsequently decreased as sites became occupied and diffusion became limiting. Equilibrium capacities increased with initial concentration, reaching 49.78, 98.34 and 132.68 mg/g, respectively.

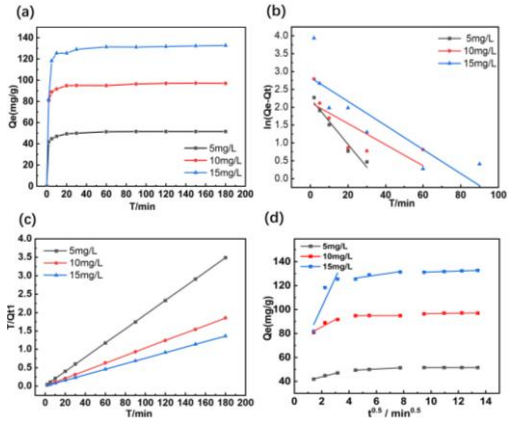

Fig. 8 Adsorption kinetics of U(VI) on ATP-CS-PA: (a) effect of contact time, (b) pseudo-first-order model, (c) pseudo-second-order model and (d) intraparticle diffusion model

The pseudo-first-order and pseudo-second-order fits are shown in Fig. 8b, c and Table 2. The pseudo-second-order model gave higher R^2 values (>0.9999) than the pseudo-first-order model (0.5838–0.9601). Its fitted equilibrium capacities (49.78–133.16 mg/g) agreed more closely with the experimental values, whereas the pseudo-first-order estimates (8.42–17.04 mg/g) were considerably lower. The fit is consistent with a substantial chemical contribution to adsorption [25].

The Weber–Morris intraparticle diffusion model [26] is shown in Fig. 8d. At each concentration, the curves contained three linear stages, all with nonzero intercepts, suggesting multiple rate-influencing processes and indicating that intraparticle diffusion may not be the sole limiting step. The first stage was attributed to film diffusion, the second to intraparticle diffusion and the third to the approach to equilibrium [27]. As the initial concentration increased from 5 to 15 mg/L, the first-stage rate constant increased from 2.9428 to 24.6089 mg/(g·min$^{0.5}$), consistent with the mesoporous structure of the material, whose most probable pore diameter was 3.8 nm [28].

Table 2 Kinetic model parameters

C_0/(mg/L)	Q_e(mg/g)	First-order kinetic model			Second-order kinetic model		
		k_1(min^{-1})	q_e(mg/g)	R^2	k^2(g/(mg·min))	q_e(mg/g)	R^2
5	49.78	0.06438	9.46	0.9601	0.02434	49.94	0.99999
10	98.34	0.02958	8.42	0.5838	0.01527	97.37	0.99997
15	132.68	0.03372	17.04	0.7378	0.0077	133.16	0.99998

3.4 Adsorption isotherms and thermodynamics

Fig. 9a shows the U(VI) adsorption isotherms of ATP-CS-PA at 298, 308 and 318 K. Adsorption capacity increased with initial concentration. At the same equilibrium concentration, capacity decreased as temperature increased, indicating an exothermic process. The Freundlich and Langmuir fits [27] are shown in Fig. 9b and c, and their parameters are listed in Table 3. At all three temperatures, the Freundlich R^2 values (0.9905–0.9968) exceeded those of the Langmuir model (0.9750–0.9896), consistent with adsorption on a heterogeneous surface. The Langmuir maximum capacity at 298 K was 526.16 mg/g.

Table 3 Isotherm parameters for ATP-CS-PA

	Langmuir			Freundlich		
Temperature (K)	q_{max} (mg/g)	KL (L/mg)	R^2	kf	1/n	R^2
298K	526.16	0.00382	0.9764	242.68395	0.20831	0.9938
308K	500.00	0.00649	0.9750	174.54978	0.28338	0.9968
318K	390.63	0.00667	0.9896	156.85942	0.24414	0.9905

Fig. 9d shows the relationship between ln K° and 1/T; the thermodynamic parameters are given in Table 4. ΔG° was negative at all three temperatures, indicating a spontaneous process [29]. Its magnitude decreased from 8.37 kJ/mol at 298 K to 7.33 kJ/mol at 318 K, suggesting reduced thermodynamic favorability at higher temperature. ΔH° was −23.71 kJ/mol, consistent with exothermic adsorption, and ΔS° was −51.21 J/(mol·K), indicating increased order at the solid–liquid interface after adsorption. Overall, U(VI) uptake by ATP-CS-PA was interpreted as a spontaneous, exothermic process dominated by coordination with contributions from weaker interactions.

Table 4 Thermodynamic parameters for ATP-CS-PA

T(K)	ΔG°(KJ/mol)	R^2	ΔH°(KJ/mol)	ΔS°(J/molK)
298	-8.36703	0.9612	-23.7122	-51.2131
308	-8.11731	0.9612	-23.7122	-51.2131
318	-7.33117	0.9612	-23.7122	-51.2131

To further assess the performance of ATP-CS-PA, its maximum adsorption capacity was compared with those of related adsorbents reported in the literature. At 298 K and pH 5.0, the

maximum capacity of ATP-CS-PA (526.16 mg/g) exceeded those of the materials listed in Table 5.

Table 5 Comparison of ATP-CS-PA with reported U(VI) adsorbents

Material	Experimental conditions	Adsorption capacity (mg/g)	
CS@ATP	PH=5.5 T=308K	159.10	[6]
CS-CMC-P-LDH	PH=5.5 T=289K	272.28	[30]
Alk-STR-$Ti_3C_2T_x$-P_1	PH=5.5 T=303K	381.67	[31]
GO-COF-V-PA	PH=5.5 T=298K	444.80	[32]
HAP/ATP	PH=4.0 T=298K	387.27	[33]
CS-SA/PCa	PH=4.0 T=298K	482.32	[34]
ATP-CS-PA	PH=5.0 T=298K	526.16	This work

3.5 Effect of adsorption–desorption cycles on U(VI) removal

The reusability of ATP-CS-PA was evaluated over five adsorption–desorption cycles using 1 mol/L HCl as the desorbent, an initial U(VI) concentration of 10 mg/L, a dosage of 0.10 g/L, pH 5.0 and 298 K. As shown in Fig. 9e, U(VI) removal decreased with cycling, from 99.78% in the first cycle to 83.48% in the fifth, retaining 84.6% of the initial removal performance. This decline may reflect irreversible occupation of some amino and phosphate sites and loss of a small amount of organic material during repeated acid desorption [35].

3.6 Effect of coexisting ions on U(VI) adsorption selectivity

Coexisting ions in uranium-containing wastewater may compete for adsorption sites or alter uranium speciation. To assess the selectivity of ATP-CS-PA, the effects of eight representative ions at 10–100 mg/L were examined at an initial U(VI) concentration of 10 mg/L (Fig. 9). The composite showed high selectivity for U(VI). Over the tested concentration range, K^+ and NH_4^+ had negligible effects on removal, which remained above 96%. The selectivity was attributed to coordination by phosphate and amino groups and the stable adsorption interface provided by ATP [36].

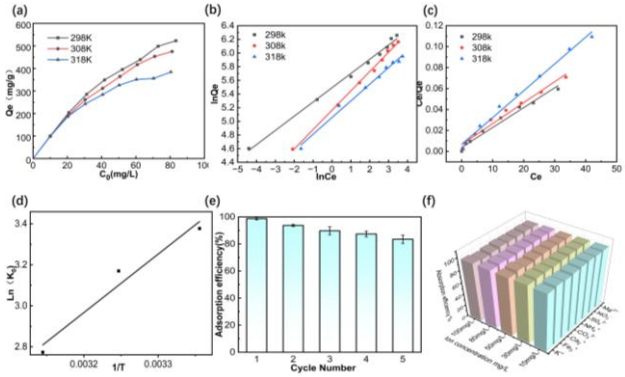

Fig. 9 Adsorption isotherms, thermodynamics, regeneration and selectivity of ATP-CS-PA: (a) effect of initial concentration, (b) Freundlich model, (c) Langmuir model, (d) ln K° versus 1/T, (e) adsorption–desorption cycles and (f) coexisting-ion tests

3.7 Adsorption mechanism

The introduction of phosphate groups was supported by EDS, FTIR and XPS. EDS showed an enhanced P signal, FTIR showed P–O bands at 1085 and 950 cm^{-1}, and XPS showed a P $2p_{3/2}$ peak at 133.5 eV assigned to phosphate groups, which shifted and broadened after adsorption. The proposed dominant role of phosphate groups can be discussed using hard–soft

acid–base theory: UO_2^{2+} is a hard Lewis acid and can preferentially coordinate with hard bases such as phosphate groups to form P–O–U bonds [37]. CS amino groups were assigned a secondary role because their shifts were smaller and their site density was lower. The shifts attributed to surface hydroxyl groups on ATP (Si–OH, Al–OH and Mg–OH) were interpreted as opposite to those of phosphate groups, suggesting different interactions with UO_2^{2+}. In the proposed interpretation, phosphate coordinates in an anionic form ($–PO_4^{2–}$), and redistribution of P–O bond electrons toward uranium increases oxygen electron density and lowers its binding energy. Hydroxyl groups act as neutral ligands, and donation of an oxygen lone pair decreases oxygen electron density and increases binding energy [38]. The proposed importance of phosphate groups was attributed to their site density and bonding strength, because each PA molecule contains six phosphate groups [39].

Three observations were used to support chemical coordination. First, at pH 2.0 the protonated, positively charged surface would repel UO_2^{2+} electrostatically, yet ATP-CS-PA retained a capacity of 46.9 mg/g, suggesting that uptake does not depend solely on electrostatic attraction [40]. Second, the positions and shapes of the P–O bands (1085 and 950 cm^{-1}) and N–H bands (1640 and 1540 cm^{-1}) changed after adsorption, consistent with interactions between U(VI) and phosphate and amino groups [41]. Third, elemental mapping showed a uniform U distribution with substantial spatial overlap with P and N and no local enrichment, consistent with coordination-based uptake [42]. These observations alone do not exclude all surface precipitation or physical retention.

The proposed mechanism is consistent with the macroscopic adsorption behavior. The pseudo-second-order fit is consistent with a chemical contribution to uptake, while $\Delta H° = -23.71$ kJ/mol and $\Delta G° < 0$ indicate exothermic and spontaneous adsorption. The better Freundlich fit is consistent with heterogeneous adsorption sites [43]. The proposed process involves P–O–U coordination by PA phosphate groups, assisted by N–U coordination of CS amino groups and interactions with surface hydroxyl groups. Uranium was assigned to the hexavalent state on the material after adsorption. A schematic is shown in Fig. 10.

The interpretation has limitations. Spatial overlap in elemental maps is correlative and does not rule out the presence of a small amount of uranium in other forms. The relative binding strengths of P–O–U and N–U coordination were not directly measured and require verification by EXAFS or theoretical calculations. It also remains unclear whether the small decrease in removal at 100 mg/L Fe^{3+}, approximately 2.5 percentage points, results from competition for sites or coverage by iron hydrolysis products.

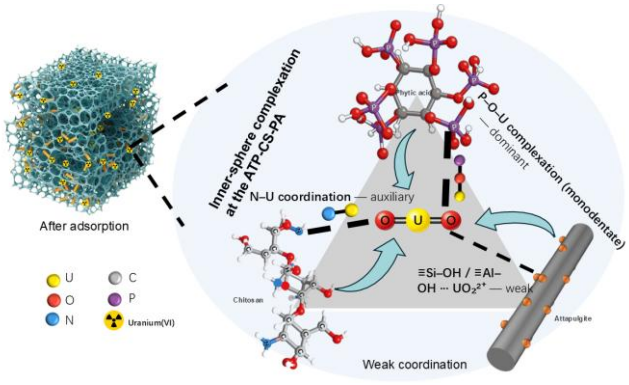

Fig. 10 Schematic of the proposed adsorption mechanism

3.8 Actual Results of Rare Earth Wastewater Treatment

To evaluate its applicability to a complex water matrix, ATP-CS-PA was applied to wastewater from in situ leaching of an ion-adsorption rare-earth ore. Samples were collected after shaking for 24 h at an adsorbent dosage of 0.10 g/L, pH 5.0 and 298 K, and ion concentrations were measured (Table 6). After adsorption, the U(VI) concentration was 0.02 mg/L, meeting the Chinese Discharge Standards of Pollutants for the Rare Earths Industry (GB 26451–2011) [44].

Table 6 Ion composition of rare-earth wastewater before and after adsorption (mg/L)

Elements	U	Pb	Cu	Zn	Fe	Al	Ba	Mg	K	Ca
Pre-adsorption	0.30	0.03	0.03	0.06	0.11	0.40	1.08	6.40	21.04	2291.58
Post-adsorption	0.02	0.03	0.02	0.06	0.10	0.36	0.88	6.33	20.64	2215.24

4 Conclusions

A ternary ATP-CS-PA composite was prepared by blending, with PA serving as both a crosslinker and a functional component. The material combines CS amino groups with phosphate sites and was designed to address the poor acid resistance and limited U(VI) selectivity of CS. The best structure and adsorption performance were obtained at an ATP:CS:PA mass ratio of 3:10:10.

At an initial U(VI) concentration of 10.00 mg/L, an ATP-CS-PA dosage of 0.10 g/L, 298 K and pH 5.0, the adsorption capacity was 98.34 mg/g. The maximum capacity fitted by the Langmuir model was 526.16 mg/g. Removal exceeded 98% in the presence of coexisting ions such as Ca^{2+} and Fe^{3+} at 10–100 mg/L, and was 83.48% after five adsorption–desorption cycles.

EDS, FTIR and XPS results were interpreted as indicating that U(VI) uptake was dominated by P–O–U coordination with PA phosphate groups, with additional contributions from CS amino groups and ATP surface hydroxyl groups.

Treatment of rare-earth wastewater initially containing 0.30 mg/L uranium reduced the U(VI) concentration to 0.02 mg/L, meeting the limit in GB 26451–2011.

Funding National Natural Science Foundation of China (Grant No. 11475080).

Data availability The data are available from the corresponding author on reasonable request.

5.Declarations

Competing interests The authors declare that they have no known competing financial interests or personal relationships that could have appeared to influence the work reported in this paper.

References

1. Patel, K. S. *et al.* Occurrence of uranium, thorium and rare earth elements in the environment: A review. *Front. Environ. Sci.* **10**, 1058053 (2023).
2. Ma, M. *et al.* Synthesis and fabrication of segregative and durable MnO2@chitosan composite aerogel beads for uranium(VI) removal from wastewater. *Water Research* **247**, 120819 (2023).
3. Liu, Y. *et al.* Facile and scalable synthesis of functionalized hierarchical porous polymers for efficient uranium adsorption. *Water Research* **257**, 121683 (2024).
4. Da Silva Bruckmann, F. *et al.* Chitosan-based adsorbents for wastewater treatment: A comprehensive review. *International Journal of Biological Macromolecules* **309**, 143173

(2025).
5. Zhang, X. *et al.* Phosphate-modified attapulgite for efficient pb(II) and cd(II) removal: surface functionalization and adsorption mechanisms. *Environ. Res.* **293**, 123751 (2026).
6. Pan, D. *et al.* Removal of uranium contaminant from aqueous solution by chitosan@attapulgite composite. *Sep. Purif. Technol.* **177**, 86–93 (2017).
7. Xia, H. *et al.* Hydrothermal fabrication of phytic acid decorated chitosan-graphene oxide composites for efficient and selective adsorption of uranium (VI). *Journal of Environmental Chemical Engineering* **11**, 110760 (2023).
8. Yang, F. *et al.* Incorporation phytic acid-modified chitosan/sodium alginate melamine sponge composite for highly efficient uranium adsorption - ScienceDirect. *International Journal of Biological Macromolecules* **318**, 145207 (2025).
9. Ding, L. *et al.* One-step synthesis of phospho-rich, silica-enhanced chitosan aerogel for the efficient adsorption of uranium(VI). *Int. J. Biol. Macromol.* **259**, 129101 (2024).
10. Su, X. *et al.* Phytate-modified MOFs grown on carbon nanotubes for efficient adsorption of uranium(VI) from seawater. *Sep. Purif. Technol.* **335**, 126102 (2024).
11. Gui, Y. *et al.* High-performance membrane for rapid and selective extraction of uranium from simulated seawater: a novel polyacrylonitrile-poly(amidoxime) hydrogel membrane material. *J. Water Process Eng.* **69**, 106732 (2025).
12. Thommes, M. *et al.* Physisorption of gases, with special reference to the evaluation of surface area and pore size distribution (IUPAC Technical Report). *Pure and Applied Chemistry* vol. 87 1051–1069 (2015).
13. Suárez, M. *et al.* Review and new data on the surface properties of palygorskite: A comparative study. *Applied Clay Science* vol. 216 106311 (2022).
14. Kaczorowska, M. A. & Bożejewicz, D. The Application of Chitosan-Based Adsorbents for the Removal of Hazardous Pollutants from Aqueous Solutions—A Review. *Sustainability* vol. 16 2615 (2024).
15. Zhang, T. *et al.* Recent developments in synthesis of attapulgite composite materials for refractory organic wastewater treatment: a review. *RSC Advances* vol. 14 16300–16317 (2024).
16. Duan, Y. *et al.* Selective adsorption of yttrium(III) and ytterbium(III) from rare earth leachate using a phytic acid ($C_6H_{18}O_{24}P_6$)-modified adsorbent. *Hydrometallurgy* **238**, 106574 (2025).
17. Zhang, Y. *et al.* Preparation of biochar@chitosan-polyethyleneimine for the efficient removal of uranium from water environment. *Carbohydr. Polym.* **312**, 120834 (2023).
18. Huang, J. Electrosorption of uranium (VI) from aqueous solution by phytic acid modified chitosan: An experimental and DFT study. *Separation and Purification Technology* https://doi.org/10.1016/j.seppur.2021.120284 (2022) doi:10.1016/j.seppur.2021.120284.
19. Peng, Q., Jin, T., Wang, C. & Qian, Y. Phytic acid-modified carboxymethyl cellulose hydrogel for uranium adsorption from aqueous solutions. *Int. J. Biol. Macromol.* **256**, 128545 (2024).
20. Krot, A. D., Tararushkin, E. V., Trigub, A. L., Vlasova, I. E. & Kalmykov, S. N. Uranium coordination on clay surface at nanoscale: Integration of EXAFS data and ab initio molecular dynamics. *Applied Clay Science* **274**, 107863 (2025).
21. Dai, Z. *et al.* Phytic acid-functionalized polyamidoxime/alginate hydrogel for targeted uranium extraction from acidic wastewater. *Carbohydrate Polymers* **339**, 122283 (2024).
22. Lei, F. *et al.* Phospho-enriched amidoxime adsorbents utilizing synergistic multifunctional groups for enhanced uranium removal from wastewater. *Chemical Engineering Journal* **488**, 151045 (2024).
23. Fazal, T., Alali, K. T., Zhu, J., Yun, X. & Wang, J. Investigating the adsorption capacity of AOPAN/CS-PVA hybrid fibrous materials for uranium (VI) extraction from seawater.

Appl. Surf. Sci. **720**, 165233 (2026).
24. Zhou, G. *et al.* Polyamidoxime-coated coconut haustorium derived magnetic biochar adsorbent with photothermal conversion for highly efficient uranium recovery from nuclear wastewater. *Adv Funct Materials* **34**, 2406329 (2024).
25. Bi, P., Chen, Y., Li, C., Jiang, Y. & Hong, W. Nitrogen and phosphorus co-doped hierarchical porous carbon for efficient uranium adsorption. *Chem. Commun.* **61**, 19921–19924 (2025).
26. Inglezakis, V. J., Fyrillas, M. M. & Park, J. Variable diffusivity homogeneous surface diffusion model and analysis of merits and fallacies of simplified adsorption kinetics equations. *Journal of Hazardous Materials* **367**, 224–245 (2019).
27. Huang, Y. *et al.* Enhancement mechanism of chitosan/tannic acid curing and functional group modification on uranium adsorption in five types of wastewater by cu-MOF. *Journal of Hazardous Materials* **492**, 138185 (2025).
28. Mei, D., Liu, L. & Yan, B. Adsorption of uranium (VI) by metal-organic frameworks and covalent-organic frameworks from water. *Coordination Chemistry Reviews* **475**, 214917 (2023).
29. Muhire, C., Zhang, D. & Xu, X. Adsorption of uranium (VI) ions by LDH intercalated with l-methionine in acidic water: Kinetics, thermodynamics and mechanisms. *Results in Engineering* **16**, 100686 (2022).
30. Li, D. *et al.* Fabrication of a chitosan/carboxymethyl cellulose composite foam with phytic acid-modified hydrotalcite for highly efficient U(VI) removal from aqueous solution. *Sep. Purif. Technol.* **386**, 136608 (2026).
31. Sheng, L. *et al.* Efficient uranium extraction by a bifunctional MXene: performance and mechanism in weakly acidic uranium mining wastewater. *J. Environ. Chem. Eng.* **14**, 121867 (2026).
32. Liu, F., Cai, J., Meng, X. & Hu, B. Phytic acid-functionalized COFs/graphene oxide composites for synergistic adsorption and immobilization of U(VI)/th(IV) from radioactive wastewater. *Colloids Surf., A* **736**, 139619 (2026).
33. Li, L. *et al.* Efficient removal of uranium (VI) by one-step synthetic environmentally friendly hydroxyapatite modified attapulgite composite material: adsorption properties and mechanism studies. *Water, Air, Soil Pollut.* **236**, 36 (2025).
34. Lei, L. *et al.* Calcium phytate cross-linked polysaccharide hydrogels for selective removal of U(VI) from tailings wastewater. *Water Research* **278**, 123343 (2025).
35. Wang, H. *et al.* Hierarchical triple-channel architectures unlock scalable and high-efficient uranium extraction from seawater. *Nat Commun* **16**, 10799 (2025).
36. Wu, H. *et al.* Phosphate/amidoxime bifunctionalized calcium alginate aerogel enabling uranium remediation under highly acidic wastewater. *Journal of Environmental Chemical Engineering* **14**, 121118 (2026).
37. Wu, H. *et al.* Phytic acid-functionalized polyacrylonitrile nanofibrous membranes via molecular self-assembly for efficient uranium extraction from highly acidic wastewater. *Separation and Purification Technology* **377**, 134361 (2025).
38. El-Seidy, A. M. A. *et al.* Mechanism of uranium(vi) sorption on α-aminophosphonate sorbents: multimodal spectroscopy and computational study. *RSC Adv.* **15**, 28269–28279 (2025).
39. Zhang, H. *et al.* Directional lamellar and underwater superelastic nanocellulose/phytic acid-functionalized chitosan aerogels for uranium extraction from seawater. *ACS Appl. Polym. Mater.* **8**, 8970–8981 (2026).
40. Liu, X. *et al.* Molecular-level understanding of metal ion retention in clay-rich materials. *Nat Rev Earth Environ* **3**, 461–476 (2022).
41. Huang, F. *et al.* Biochar-mediated remediation of uranium-contaminated soils: Evidence,

mechanisms, and perspectives. *Biochar* **6**, 16 (2024).
42. Zhao, X., Chen, D., Shi, M. & Zhao, R. Anchoring chitosan/phytic acid complexes on polypyrrole nanotubes as capacitive deionization electrodes for uranium capture from wastewater. *International Journal of Biological Macromolecules* **270**, 132491 (2024).
43. Murphy, O. P., Vashishtha, M., Palanisamy, P. & Kumar, K. V. A review on the adsorption isotherms and design calculationsfor the optimization of adsorbent mass and contact time. *ACS Omega* **8**, 17407–17430 (2023).
44. Wu, X. *et al.* Highly acid-stable polyvinyl alcohol/chitosan/phytic acid aerogel for selective separation of uranium from actual wastewater. *Journal of Environmental Chemical Engineering* **12**, 113358 (2024).